Journal of Applied Fluid Mechanics, Vol. 18, No. 4, pp. 1007-1022, 2025.
Available online at www.jafmonline.net, ISSN 1735-3572, EISSN 1735-3645.
https://doi.org/10.47176/jafm.18.4.2963

Experimental Study on Separated-flow Transition on a High-lift Blade

S. Yang[1], F. Tian[1], C. Teng[2] and B. Xu[1†]

[1] *School of Energy and Power Engineering, Dalian University of Technology, Dalian, Liaoning, 116024, China*
[2] *Commercial Aircraft Corporation of China Ltd, Shanghai, 2001126, China*

†*Corresponding Author Email: Baopengxu@dlut.edu.cn*

ABSTRACT

The increasing loading level for high-lift blades in low-pressure turbines leads to a laminar separation bubble (LSB) formed on the surface, resulting in a greater profile loss. To obtain a detailed understanding of the flow physics, experiments were conducted at various Reynolds numbers (*Re*) using complementary hot-wire and hot-film anemometers. Two instability regions are confirmed inside/outside the LSB. The external region is due to the inviscid Kelvin–Helmholtz (K–H) instability, while the internal one originates from the reversed-flow even at a low reversal level. The Strouhal number associated with K–H instability remains constant as *Re* changes. Furthermore, the modal instability primarily in the form of the K–H mechanism and the non-modal instability due to the streamwise streaks induced by the freestream turbulence (FST) are found to coexist. The non-modal instability contains mainly low-frequency fluctuating energy, which impacts the disturbance energy spectrum within the separated shear layer. This reveals that the inflectional velocity profiles amplify the fluctuating energy within both the K–H frequency band and the low-frequency range. The origin of the latter can be traced upstream of the separation. However, inflectional instability remains immanently linked to the inviscid K–H instability, which cannot be bypassed as *Re* increases even with a thinner LSB.

Article History

Received July 2, 2024
Revised October 7, 2024
Accepted November 3, 2024
Available online February 4, 2025

Keywords:

Low-pressure turbine
Laminar separation bubble
K-H instability
Non-modal instability
Viscous instability

1. INTRODUCTION

High-lift blades have been used to reduce the weight of low-pressure turbines. The large adverse pressure gradients at the rear of high-lift blades render the boundary layer susceptible to separation, resulting in severe aerodynamic losses (Howell et al., 2000). The most widespread application is the "calmed-region" effect, which increases the lift of a low-pressure turbine blade by 20%~30% without sacrificing efficiency, and has been used in engines such as the BR710/715 and Trent500/900 (Howell et al., 2002; Hodson & Howell, 2005). Despite significant achievements over the past few decades, the underlying mechanisms of flow behaviors in low-pressure turbines remain partially elusive, especially the separated-flow transition.

Mayle (1991) presented a comprehensive review of laminar-turbulent transitions in gas turbines, categorizing the transition modes into natural transition, bypass transition, separated-flow transition, periodic-unsteady transition (also known as wake-induced transition), and reverse transition. The first three of these transition modes are discussed in the present study. In a low-disturbed attached boundary layer, the transition mode typically manifests as a natural transition, whose mechanisms have been extensively studied. Small disturbances in the laminar boundary layer gradually evolved into a two-dimensional (2D) Tollmien–Schlichting (T–S) wave and ultimately developed into turbulent spots. The bypass transition has been thoroughly investigated (Jacobs & Durbin, 2001; Zaki & Durbin, 2005, 2006). Disturbances penetrate into the boundary layer through a "shear sheltering" effect, inducing streamwise streaks. These streaks become unstable through sinuous or varicose modes (Zhao & Sandberg, 2020), eventually developing into turbulent spots characterized by a broad frequency spectrum. Separated-flow transition is more intricate than the above two mechanisms. Gaster (1967) termed the region including separation and reattachment a laminar separation bubble (LSB). Mayle (1991) indicated that the LSB is typically accompanied by a transition. Therefore, in the present study, an LSB refers to a bubble with laminar separation followed by turbulent reattachment. Although Mayle (1991) classified the separated-flow transition as a distinct mode, it is not actually a new

NOMENCLATURE

PSD	Power Spectral Density	f	frequency of K-H instability
RMS	Root Mean Square	H_{12}	shape factor
LSB	Laminar Separation Bubble	Re	Reynolds number
C	chord length	Sr	Strouhal number.
C_x	axial length	N	sample length
C_p	static pressure coefficient	E	voltage of the hot film with flow
Z_w	Zweifel coefficient	E_0	voltage of the hot film without flow
g	cascade pitch	C_τ	normalized mean quasi-wall shear stress
g^*	non-dimensional pitchwise distance	α	inlet angle
x	cascade axial coordinate	β	outlet angle
y	normal to the wall direction	δ	nominal thickness
p_0	total pressure	δ^*	displacement thickness
p	static pressure	θ	momentum thickness
p_i	static pressure along the surface	ρ	air density
Δp^*	non-dimensional total pressure loss	ζ	profile loss of the cascade
u	velocity profile of the boundary layer	τ_n	quasi-wall shear stress
U	outlet velocity	v	kinematic viscosity
U_e	velocity at the boundary layer edge	**Subscripts**	
u_{ref}	freestream velocity at the trailing edge	*1*	inlet plane
u_{rms}	root mean square of the velocity	*2*	outlet plane
f_1	upper limit of the PSD integral	*e*	the edge of the boundary layer
f_2	lower limit of the PSD integral	*s*	position of the separation point

transition mode but a combination of the others under different conditions (e.g., Reynolds number (*Re*), turbulence intensity, and surface roughness). Further descriptions are provided below to illustrate the effect of freestream turbulence on separated-flow transition.

When the freestream turbulence (FST) intensity is low, with the coexistence of both attached and separated boundary layers, the transition may exhibit both the viscous T–S and the inviscid K–H instability mechanisms. It is still not fully understood which mechanism dominates this transition. Lang et al. (2004) used an oscillating wire to generate 2D artificial disturbances and conducted laser doppler velocimetry (LDV) and particle image velocimetry (PIV) experiments to investigate the LSB. They concluded that the T–S mechanism dominated the transition flow. Similar conclusions were drawn from linear cascade experiments (Volino, 2002b; Volino & Bohl, 2004), in which the T–S instability frequency predicted by Walker (1989) was observed. By contrast, Spalart and Strelets (2000) and Yang and Voke (2001) observed the K–H instability governing the transition via numerical simulations. Researchers have proposed complex interactions between these two instability mechanisms (Brinkerhoff & Yaras, 2011; Hain et al., 2009; Marxen, 2020; Rist & Maucher, 2002). Watmuff (1999) demonstrated that the boundary layer is viscously stable to small-magnitude disturbances while attached; however, after separation, growth in wave amplitude occurs in the detached shear layer owing to the inviscid K–H instability. Numerical simulations by McAuliffe and Yaras (2008) and Roberts and Yaras (2005), and Singh (2019) found that the T–S instability predominantly governs the disturbance growth after separation, whereas K–H instability is associated with the roll-up and shedding of spanwise vortices within the detached shear layer. Additionally, both instabilities occurred at the same frequency, suggesting a potential interaction between them, which is consistent with the findings of Hain et al. (2009). However, other studies have shown an independent relationship between the T–S and K–H mechanisms during separated-flow transition (Funazaki et al., 2009), as two distinct peaks exist in the frequency domain and correspond to the viscous and inviscid instability modes, respectively. Brinkerhoff and Yaras (2011) revealed that the interaction between the viscous and inviscid instability modes contributes to the formation of hairpin-like vortices. Diwan and Ramesh (2009) demonstrated that the inviscid inflectional instability of the separated shear layer was supposed to be logically viewed as a continuation of the instability within upstream attached boundary layer undergoing adverse pressure gradient. They concluded that a K–H instability could only be activated when the separated shear layer departs significantly from the wall.

As the FST intensity increases, the instability mode in the separated shear layer is altered. Hosseinverdi and Fasel (2019) used a series of highly resolved direct numerical simulation (DNS) to investigate the physical mechanisms dominating the transition in LSBs. They proposed that the separated-flow transition was determined by the interaction between the low-frequency Klebanoff mode (induced by the FST) and the K–H mode (enhanced by the FST). The dominance of the two modes was contingent on FST intensity. Jaroslawski et al. (2023) revealed the coexistence of modal instability due to LSB and non-modal instability caused by Klebanoff streaks. However, whether the K–H instability become entirely bypassed when non-modal instability (Klebanoff mode) dominates the transition? Yang (2019) concluded that the K–H instability stage cannot be bypassed if the LSB is induced by adverse pressure gradients. The absence of K–H instability implies total suppression on the LSB. These conclusions are supported by Balzer and Fasel (2016), Li and Yang (2016), and Istvan and Yarusevych (2018). Furthermore, the streaks within the separated shear layer distorted the spanwise vortices generated by the K–H

instability, accelerating the K–H vortices into chaotic 3D structures. Despite the K–H instability not being bypassed, streamwise streaks play a crucial role in the separated-flow transition (Istvan & Yarusevych, 2018). Elevating the FST intensity results in streamwise streaks convecting through the shear layer, and the receptivity mechanism which leads to the shear layer roll-up being bypassed (McAuliffe & Yaras, 2010). The intense shear stress linked to the streaks appears to foster environments favorable for turbulent spot formation due to a localized secondary instability, the frequency of which closely matches that of the inviscid K–H mode in a free-shear layer. This finding is also supported by Coull and Hodson (2011).

In addition to the instability in the separated shear layer, an instability region exists within the LSB, which is attributed to the reversed-flow. Rist and Maucher (2002), employing linear stability theory and DNS, identified two distinct instability regions inside and outside the separation bubble. The external flow is unstable via inviscid instability, whereas in the reversed-flow region near the wall, a viscous instability is present. The dominance of the two instabilities depended on the distance of the separated shear layer from the wall and the reversal level. McAuliffe and Yaras (2008) reported similar findings. The near-wall instability has also been observed in a low-speed linear cascade through numerical simulations and experiments (Bolinches-Gisbert et al., 2020). However, these results were not consistently replicated in some experiments conducted in a turbine cascade (Funazaki et al., 2009; Satta et al., 2014; Volino, 2002a), suggesting that the conditions leading to the near-wall instability are not completely clear. Increasing the reversal level can result in absolute instability, which can propagate upstream and become self-sustaining. According to Alam and Sandham (2000) and Rist and Maucher (2002), a reversal level exceeding 15%~20% of the local freestream velocity triggered absolute instability. Moreover, other studies (Rodríguez et al., 2013; Rodríguez et al., 2021; Rodríguez & Gennaro, 2019) have reported global instability in the LSB. For a 2D bubble, a lower reversal velocity of approximately 12% triggers absolute instability, whereas for a three-dimensional (3D) bubble, the threshold decreases to approximately 7%.

Hot-film probes are widely recognized as crucial tools for investigating the boundary layer transition owing to their high sampling rate and non-intrusive nature. Using hot-film probes, Liang et al. (2015), Mahallati et al. (2012) and Zhang et al. (2002) conducted extensive researches on the boundary layer transition. Nevertheless, inconsistencies persist in the interpretation of the results, particularly regarding the effectiveness of hot-film probes for directly detecting transition signals in the separated shear layer. This complexity is further compounded when an instability region exists inside the separation bubble, which is an aspect yet to be explored. Given the limitations of hot-wire probes near walls, combining them with hot-film sensors can enhance the experimental accuracy.

As it is difficult to perform detailed measurements in the boundary layer, most researchers opt for a flat plate or NACA airfoil operating under adverse pressure gradients.

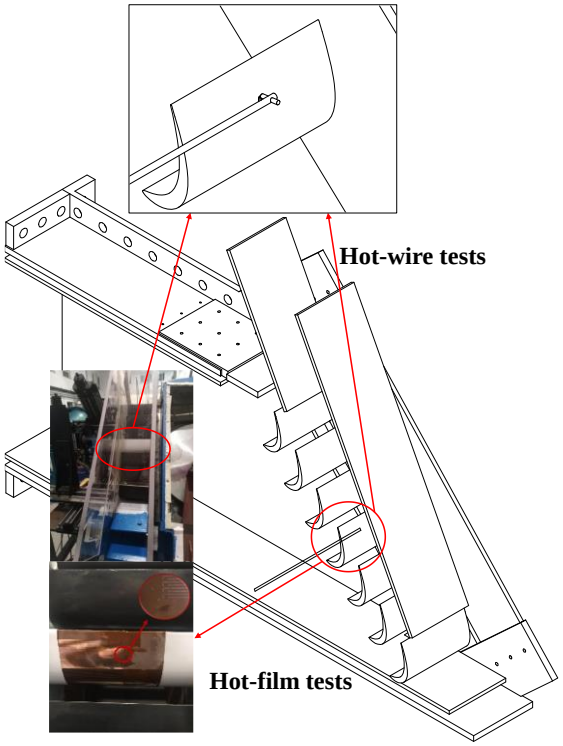

Fig. 1 Linear cascade test apparatus

Few studies have been conducted on actual low-pressure turbine blades. In this study, experiments were carried out in the cascade wind tunnel laboratory at Dalian University of Technology. The boundary layer flow was investigated using both hot-wire and hot-film probes. The primary objective of this study was to examine the disturbance growth and transition mechanisms in a separated boundary layer under different *Re* conditions. The remainder of this paper is organized as follows. Section 2 outlines the experimental setup and data processing methods. Section 3 presents the experimental results. Finally, Section 4 concludes the paper.

2. EXPERIMENTAL SETUP AND MEASUREMENT METHODS

2.1 Experimental Configuration

Fig. 1 shows a schematic of the experimental configuration used in this study. The linear cascade consists of seven high-lift blades with a Zweifel coefficient of 1.2. Hot-wire and hot-film tests were performed on the middle blade. Blade details are listed in Table 1, and the definitions are shown in Fig. 2, with Blade 1 serving as the datum blade. The Zweifel coefficient Z_w is defined as follows:

$$Z_w = 2g\cos^2\beta(\tan\alpha - \tan\beta)/C_x \quad (1)$$

A blade with a Z_w larger than 1.0 can be seen as a high-lift blade. Therefore, Blade 2 is a high-lift blade, and Blade 1 is an ordinary blade.

The experiments were conducted in an open-circuit wind tunnel with a contraction ratio of 9:1 driven by a centrifugal compressor. The inlet and outlet of the entire

Table 1 Geometric properties of the cascades

Property	Blade 1[1]	Blade 2
α(°)	42.8	42.8
β(°)	62.7	62.7
C/g	1.4256	1.142
C_x/g	1.339	1.007
Z_w	0.9	1.2
C_x(mm)	100	100

[1]Blade 1 is the datum blade

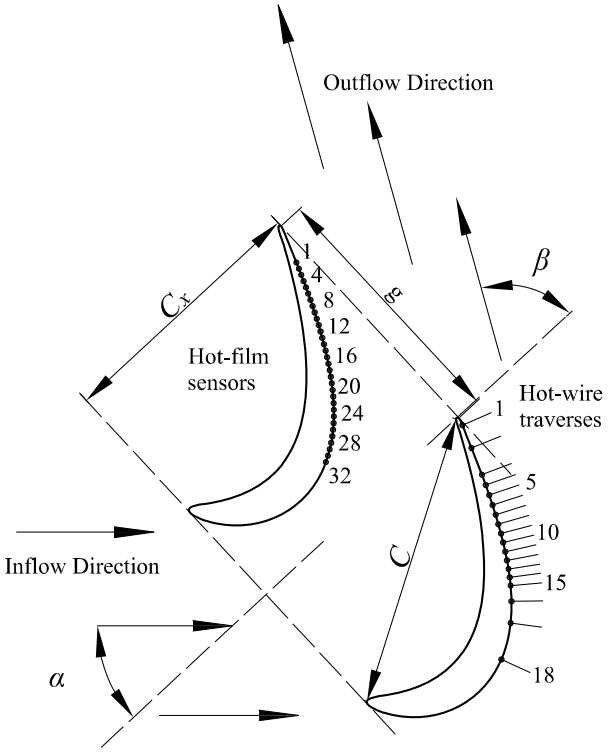

Fig. 2 Definitions of the geometric properties and schematics of the hot-wire and hot-film tests

configuration were confined within the laboratory, which can provide steady conditions. This provides a continuously adjustable freestream velocity ranging from 5 to 40 m/s. The dimensions of the test section are 590 mm × 180 mm, which ensures a uniform inflow in the pitchwise direction and minimizing the endwall effect. All tests were performed at the midspan plane of the blade. The FST intensity was 1.2%, with a fluctuation of 0.1%. Details of the aerodynamic tests can be found in Yang et al. (2023).

The pressure signals were acquired using a Scanivalve DSA 3217. A three-axis computer-controlled traversing mechanism with a stepping accuracy of 0.005 mm was utilized to ensure precise movement. In the hot-wire and hot-film tests, the measured blade was replaced with a 3D-printed resin blade to reduce the heat exchanging effect (Ikeya et al., 2017), and a smooth surface was ensured using stereolithography (SLA) technology with a roughness Ra = 1.5 μm. The suction side boundary layer was surveyed by 18 traverses normal to the surface, covering 49%~99% of the axial chord length, as shown in

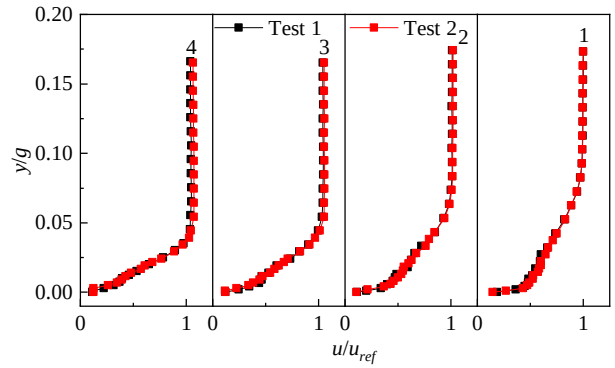

(a) Velocity profiles

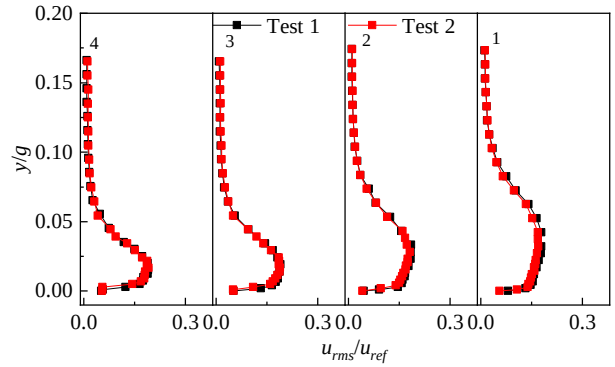

(b) Unresolved unsteadiness profiles

Fig. 3 Experimental reproducibility verification (Re = 1.2×10^5)

Fig. 2. The enlarged insert in Fig. 1 illustrates the hot-wire probe manipulation on the blade surface. The traverses were refined in the separation region, with each traverse having a minimum height of 12 mm. A Hanghua CTA-02A multi-channel hot-wire anemometer system was employed, operating the hot-wire probe in constant-temperature mode with an overheat ratio of 1.2. The output voltages were sampled via NI data acquisition, collecting 100,000 samples per measuring point at a sampling frequency of 20 kHz, ensuring adequate frequency resolution for spectrum analysis. The hot-wire experiments included 18 traverses divided into five groups. The hot-wire probe was calibrated twice, at the beginning and end of each group. The data were considered valid only when two calibrations were consistent. The first group, comprising traverses 1~4, was tested twice to verify whether this method could replicate the experiments. The results are shown in Fig. 3. An array of 32 individual surface-mounted hot-film sensors (SENFLEX9102 from TAO SYSTEM) with an equally spaced interval of 2.54 mm (0.1 in) was employed on the surface of Blade 2. Both the hot-wire probe and hot-film sensors were operated using the same setup. The boundary layer traverses and hot-film sensors locations, along with their reference numbers, are shown in Fig. 2 and summarized in Table 2 and Table 3, respectively.

2.2 Data Processing

The profile loss ζ and static pressure coefficient C_p are given as follows:

Table 2 Hot-wire traverse positions

Station	x/C_x (%)	Station	x/C_x (%)	Station	x/C_x (%)
1	99.1	7	85.2	13	74.7
2	95.8	8	83.5	14	72.8
3	91.7	9	81.8	15	71.0
4	90.1	10	80.1	16	67.2
5	88.5	11	78.3	17	61.2
6	86.8	12	76.5	18	49.2

Table 3 Hot-film sensor positions

Station	x/C_x (%)	Station	x/C_x (%)	Station	x/C_x (%)
1	94.8	12	83.6	24	67.0
4	92.0	16	78.8	28	59.7
8	88.0	20	73.3	32	51.2

$$\zeta = (p_{01} - p_{02})/(0.5\rho U^2) \tag{2}$$

$$C_p = (p_1 - p_i)/(p_{01} - p_2) \tag{3}$$

The time-averaged u and root-mean-square u_{rms} velocities obtained from the hot-wire probes were normalized using the freestream velocity u_{ref} at the trailing edge. The integral parameters of the boundary layer are calculated as follows:

$$\delta^* = \int_0^\delta (1 - u/U_e)dy \tag{4}$$

$$\theta = \int_0^\delta u/U_e(1 - u/U_e)dy \tag{5}$$

$$H_{12} = \delta^*/\theta \tag{6}$$

where δ represents the boundary layer nominal thickness, where the velocity reaches 99% of the freestream velocity. To simplify the experiments and ensure the accuracy of the integral parameters, a spline fit was applied to the velocity profile (Coull & Hodson, 2011). The maximum deviation between the spline-fitted and measured profiles was below 1%, and the maximum deviation of the calculated integration parameters was below 5%. This process also aids in identifying the inflection point of the velocity profile.

The power spectral density (PSD) of the fluctuating velocity was evaluated at each measurement point by averaging 23 fast Fourier transform (FFT) performed on data blocks with 50% overlap. With a data sample length of 8192, a frequency resolution of 2.44 Hz was obtained. To analyze the correlative contributions of the different frequency ranges, the summation of the spectral energies within the designated frequency bins was calculated by Eq. 7. Additionally, the kinetic energy related to the disturbance within the corresponding frequency range was quantified.

$$\int_{f_1}^{f_2} SDdf \quad P = (u_{rms})^2|_{f_1}^{f_2} \tag{7}$$

Hot-film calibration poses a significant challenge, and even after calibration, a 20% error remains in the data between laminar and turbulent flows (Davies & Duffy, 1995). Consequently, the semi-quantitative wall shear stress τ_n, (Hodson, 1985) is practically employed. τ_n and other statistical quantities (i.e., τ_{mean}, τ_{rms}, and τ_{skew}) are expressed as follows:

$$\tau_n = \left((E^2 - E_0^2)/E_0^2\right)^3 \tag{8}$$

$$\tau_{mean} = 1/N \sum_{n=1}^{N} \tau_n \tag{9}$$

$$\tau_{rms} = \sqrt{1/N \sum_{n=1}^{N} (\tau_n - \tau_{mean})^2} \tag{10}$$

$$\tau_{skew} = 1/(N\tau_{rms}^2) \sum_{n=1}^{N} (\tau_n - \tau_{mean})^3 \tag{11}$$

The signal mean, root mean square (RMS), and skewness quantify the time average level, fluctuation intensity, and asymmetry of the signal fluctuation, respectively. These statistical quantities provide insight into the boundary layer state.

To facilitate comparison across various flow conditions, the mean quasi-wall shear stress τ_n was further normalized in C_τ, which is defined as:

$$C_\tau = (\tau_{mean} - \tau_{min})/(\tau_{max} - \tau_{min}) \tag{12}$$

where τ_{max} and τ_{min} are the maximum and minimum values along the entire hot-film array for each *Re* number.

2.3 Uncertainties

The uncertainty calculation of the experimental data was performed in accordance with the results of BIPM et al. (2008) and Sun et al. (2020). Scanvalve DSA 3217 was used to measure the pressure data with a ±0.12% full-scale accuracy. The stochastic error was minimized by averaging the signals for a period of approximately 20 and 5 s for the pressure and thermal sensor measurements, respectively. The primary parameter uncertainties are listed in Table 4. The closest hot-wire probe distance to the wall was ensured to be lower than 0.01 mm via a handheld microscope. The wall distance uncertainty was ±0.05 mm. Hot-film sensors were not calibrated during the experiments.

Table 4 Parameter uncertainties

Parameter	Uncertainty (%)
Inlet Velocity	±1.7
Static pressure coefficient C_p	±3.5
Profile loss ζ	±3.5
Velocity u	±2
Displacement thickness δ^*	±3.5
Momentum thickness θ	±5
Shape factor H_{12}	±6.1

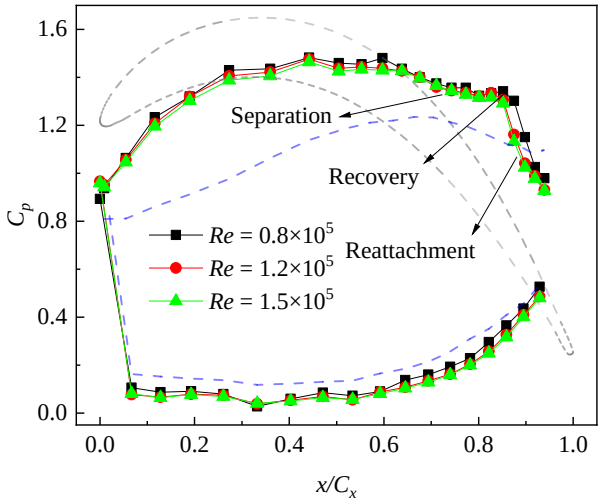

Fig. 4 Static pressure distributions of Blade 2. For reference, the blue dashed line denotes the static pressure distributions for Blade 1 at *Re* = 1.2×10^5

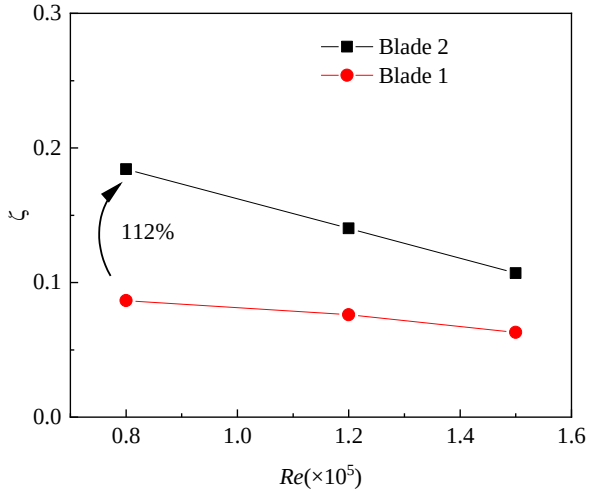

Fig. 5 Profile loss of Blade 2 with varying *Re*. Blade 1 is shown for reference

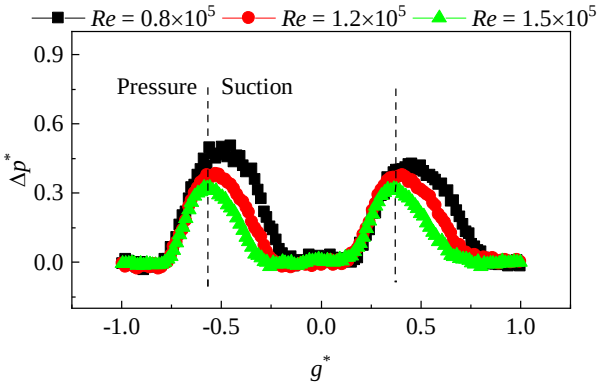

Fig. 6 Pitchwise distributions of the total pressure loss of Blade 2

3. RESULTS

3.1 Aerodynamic Performance of the Blades

The loading distributions of Blade 2 according to C_p are shown in Fig. 4, exhibiting a mid-loading profile with flat loading distributions around the peak. Compared with ordinary Blade 1, the loading level was substantially enhanced. However, downstream of the loading peak, a "plateau" emerges, which is a typical indicator of boundary layer separation. The pressure coefficients at the trailing edge indicate that reattachment was accomplished at all *Re* numbers. Furthermore, there is a reduction in the LSB size as *Re* increases.

As shown in Fig. 5, the high-lift blade suffers a greater profile loss compared to the datum blade. At the lowest *Re*, this disparity reaches up to 112%. As *Re* increases, the loss decreases and the disparity diminishes. The pitchwise distributions of total pressure loss are shown in Fig. 6, where Δp^*denotes the total pressure loss normalized by the outlet dynamic pressure, and g^* is the pitchwise distance normalized by the cascade pitch. These results indicate that *Re* mainly affects the suction side losses, with minimal impact on the pressure side. It can be inferred that the LSB on the suction side is the main factor affecting the aerodynamic performance of the high-lift blades. Accordingly, detailed separated boundary layer measurements are presented next.

3.2 Velocity Profiles

Hot-wire probes were employed to investigate the boundary layers. The normal distance y from the surface was normalized by the cascade pitch g, while the time-averaged velocity was normalized by the freestream velocity u_{ref} at the trailing edge. A deficit in the velocity profile indicates separation, whereas the region in which the inflection of the velocity profile vanishes and begins to become fuller denotes a reattachment point. As shown in Fig. 7, the separation and reattachment locations approximately align with the loading distributions. Errors mainly stem from the resolution deviation of the measurement traverses and pressure taps. The separation bubble extends as *Re* decreases. However, the maximum separation bubble thickness under different conditions was approximately 83.5%C_x. It is noteworthy that a larger *Re* only slightly delays the separation, but considerably advances the reattachment, which also leads to a difference in the boundary layer state at the trailing edge. As seen from stations 1~3, the apparent divergences between the velocity profiles demonstrate that the velocity profiles become fuller as *Re* increases. It should also be noted that placing the hot-wire probe within the separated shear layer did not have a significant effect on the LSB.

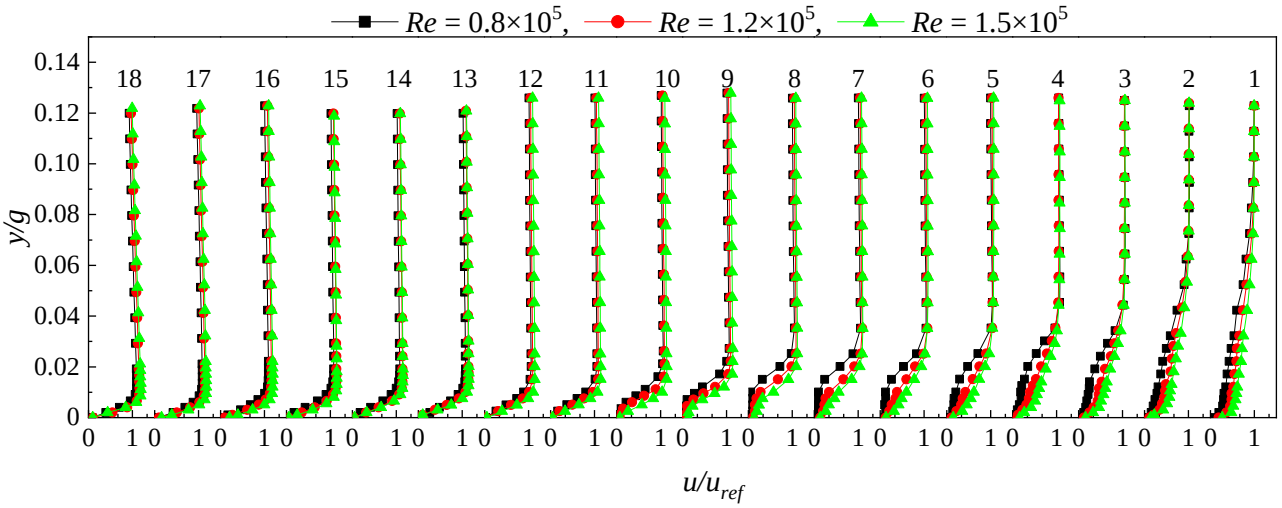

Fig. 7 Non-dimensional mean velocity profiles

Table 5 Separation and reattachment point locations

Re (×10^5)	Separation points		Reattachment points	
	Loading distribution (x/C_x)	Hot-wire (x/C_x)	Loading distribution(x/C_x)	Hot-wire(x/C_x)
0.8	74.3%	74.7%	91.9%	91.7%
1.2	74.3%	76.5%	89.8%	88.5%
1.5	77.3%	78.3%	87.5%	86.8%

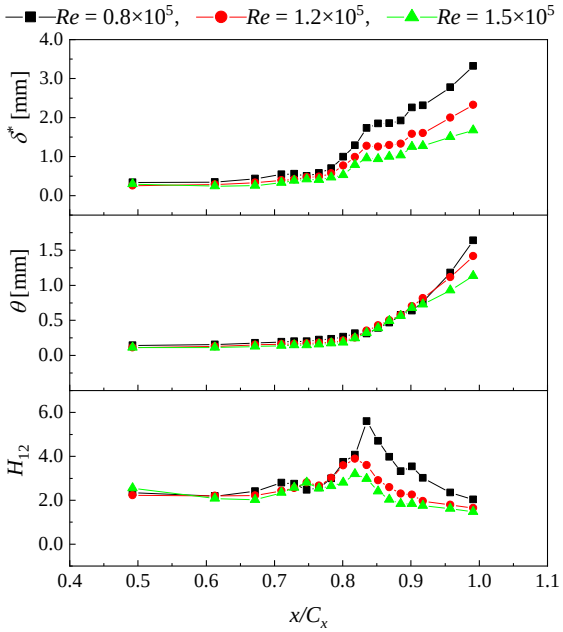

Fig. 8 Integral parameters distributions along the suction side

When a hot-wire was introduced inside the bubble, its shape and size were modified. However, the hot-wire effect on the LSB was not quantified in the present study according to Diwan and Ramesh (2009).

3.3 Integral Parameters

As shown in Fig. 8, the boundary layer integral parameters followed a similar trend at different *Re*. The displacement thicknesses δ^* sharply increase after separation, while the momentum thicknesses θ do not experience large variations. A "plateau" is noted in the mid-to-rear section of the LSB, after which the displacement thickness continues to grow. This differs from the experimental results for a flat-plate boundary layer under adverse pressure gradients. The momentum thickness curves exhibited minimal deviation before 90%C_x. According to Denton (1993), momentum thickness is a good indicator of profile loss. As *Re* increases, a large reduction in the profile loss is achieved, which is consistent with the results shown in Fig. 5. The boundary layers remained laminar before separation because the shape factors were larger than two. The maximum value occurred at approximately 83%C_x, slightly advancing at higher *Re*, indicating that reattachment occurred. This is consistent with the recovery positions observed in the C_p distributions. For *Re* = 0.8×10^5, the shape factor experiences a steep decrease after the maximum value until the trailing edge, which indicates that the laminar-turbulent transition is not yet complete. By contrast, in the other two cases, the shape factors remain almost constant near the end, suggesting fully developed turbulent boundary layers.

Because of the challenge of manipulating hot-wire probes on the blade surface, it is difficult to ensure the desired precision of the probe-to-wall distance. However, the evolving trends and differences reflected by the integral parameters remain of interest. The effects of *Re* on the separation and reattachment points are summarized in Table 5.

3.4 Unresolved Unsteadiness Distributions

With the high sampling rate of the hot-wire anemometer, the unresolved unsteadiness was estimated using the root mean square of the velocity, which can reveal the level of fluctuations in the boundary layer. The

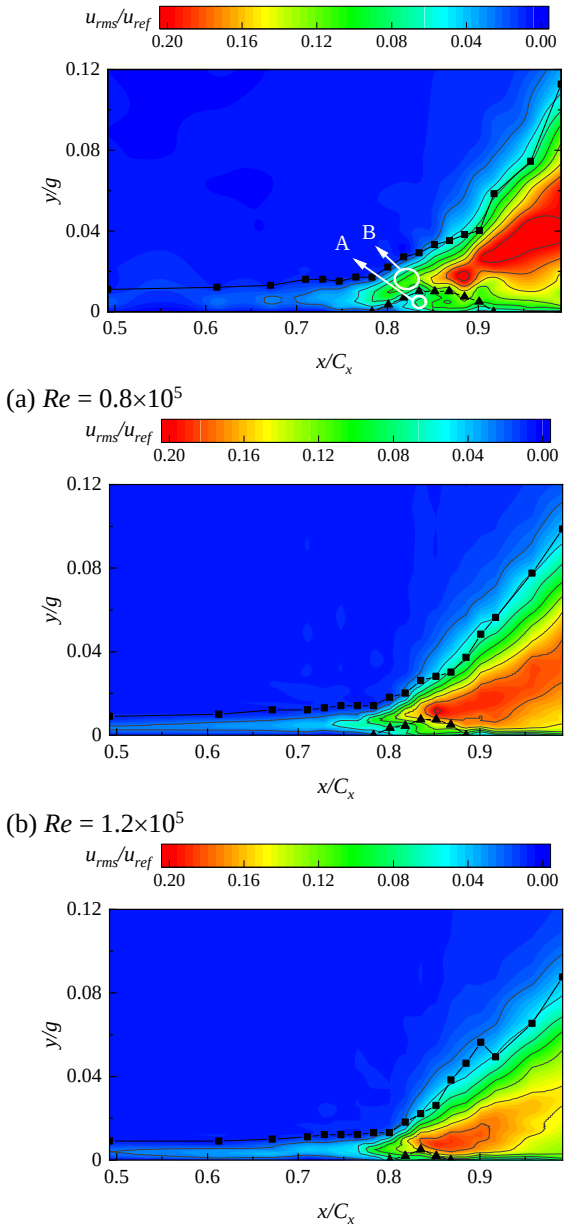

(a) $Re = 0.8\times10^5$

(b) $Re = 1.2\times10^5$

(c) $Re = 1.5\times10^5$

Fig. 9 Unresolved unsteadiness contours in the boundary layer. The square symbols represent the boundary layer edge, and the triangular symbols denote the separation bubble edge

u_{rms} profiles measured by the hot-wire probe were also spline-fitted with an interval of 0.1 mm to generate the contours. Data from y = 0~12 mm for 18 traverses were selected. The results were also normalized by u_{ref}. As shown in Fig. 9, the perturbations originate upstream of the separation but with a low growth rate. After reaching separation, owing to the LSB, the perturbations are lifted into the separated shear layer, the growth rate of which increases noticeably and eventually leads to breakdown. In addition to the perturbations (Region B) within the separated shear layer, a fluctuation peak (Region A) is observed near the wall inside the bubble, as shown in Fig. 9(a). This finding is typically reported for a flat-plate boundary layer, as observed in the experimental results of Lang et al. (2004) and the numerical results of Mcauliffe and Yaras (2010). However, this has rarely been observed

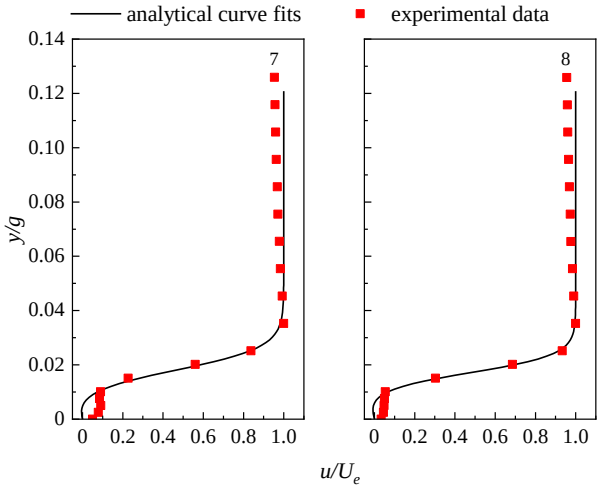

Fig. 10 Comparison between the analytical curve fits and experimental data ($Re = 0.8\times10^5$)

in turbine blade experiments. The perturbations in Region A could be a consequence of near-wall viscous instability or absolute instability due to the reversed-flow. The stationary hot-wire probe is insensitive to the flow direction, posing restrictions for exploring reversed-flows. Therefore, the hyperbolic-tangent velocity profile model modified by Diwan and Ramesh (2009) was employed to obtain a curve fit for the measured mean velocity profile. They noted that the near-wall hot-wire uncertainty present no serious problem in fitting the analytical curves. The outcomes are validated in Fig. 10, the analytical fits are in good accordance with the measurements at stations 7 and 8, where the separation bubble thickness is at its maximum. Curve fitting in the present study was only applied to estimate the reversed-flow intensity. The maximum reversal velocity, as indicated by the analytical fits, was < 1% of the local freestream velocity. Considering that the minimum threshold for absolute instability is 7%, it can be concluded that absolute instability did not occur in the present experiments. The near-wall perturbations are still visible in Fig. 9(b), which are not as clear as in the low-*Re* case, and they are nearly absent at the highest *Re*, as shown in Fig. 9(c), due to the thinner bubbles.

Instability in a free shear layer is primarily attributed to the inviscid K–H mechanism, which is characterized by a specific frequency range. The dominant frequency was standardized as the Strouhal number (Sr). The formula $Sr_{\theta s} = f\theta_s/U_{es}$ adopted by Mcauliffe and Yaras (2010) is used to calculate $Sr_{\theta s}$. As shown in Fig. 11, the frequency spectrum at different streamwise positions along the separated shear layer reveal an increase from 500 to 1000 Hz as *Re* changes. However, $Sr_{\theta s}$ remains nearly constant. Table 6 lists the dominant $Sr_{\theta s}$ obtained in the present study, alongside those documented in other experimental and numerical investigations. This demonstrates that the instability in the separated shear layer (Region B) was driven by inviscid K–H mechanism. The specific frequency of the T–S wave predicted by Walker (1989) was not discerned within the low-frequency range.

It is noteworthy that the power spectral density (PSD) in Fig. 11 was obtained from the upper location within the

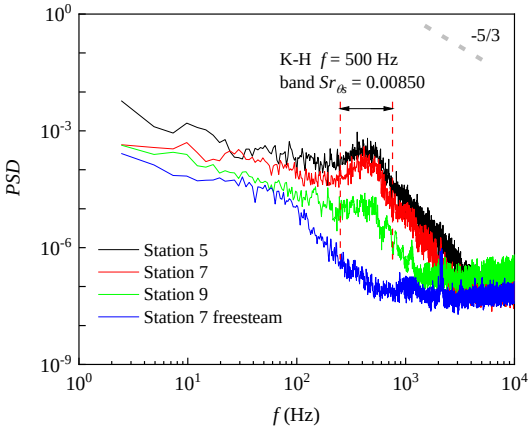

(a) $Re = 0.8\times10^5$

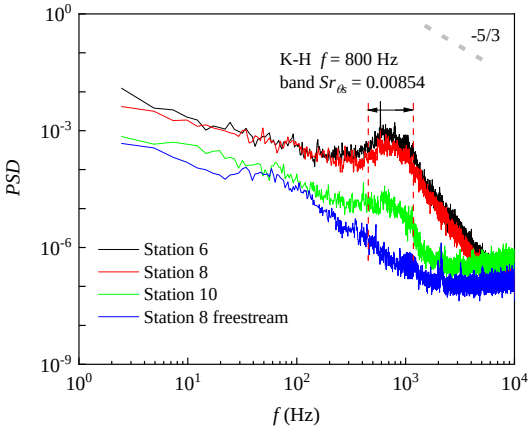

(b) $Re = 1.2\times10^5$

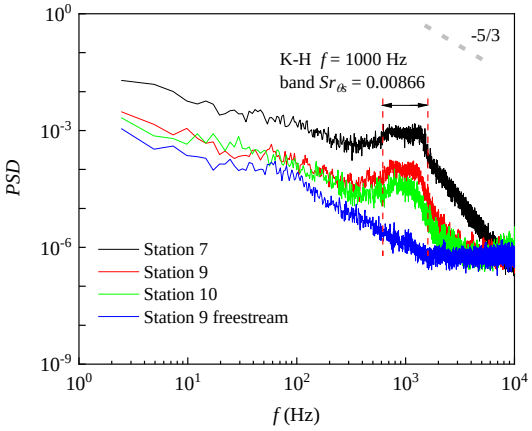

(c) $Re = 1.5\times10^5$

Fig. 11 Power spectral density of the velocity in the separated shear layer

separated shear layer because the K–H frequency bands were more pronounced than those at the inflection points. However, this does not imply that the K–H instability becomes inactive within the separated shear layer. There are two possible explanations for this observation. First, because of the FST in the inlet, the LSB tended to be relatively thin. As demonstrated by Diwan and Ramesh (2009), a description of the K–H instability paradigm becomes relevant only when the separated shear layer moves considerably away from the wall. Thus, the K–H instability at the inflection point of the shear layer may not be intense owing to its proximity to the wall (approximately 1 mm at the maximum). Second, there is another mechanism known as non-modal instability (also

Table 6 Characteristic shear layer instability $Sr_{\theta s}$ in the literature

Ref.	$Sr_{\theta s} = f\theta_s/U_{es}$
Present study	0.0085~0.0087
Mcauliffe and Yaras (2010)	0.011
Mcauliffe and Yaras (2005); Mcauliffe (2007)	0.008~0.016
Lin and Pauley (1996); Ripley and Pauley (1993)	0.005~0.008
Yang and Voke (2001)	0.005~0.011
Talan and Hourmouziadis (2002)	0.010~0.014
Ho and Huerre (1984) (free-shear)	0.016

referred to as the Klebanoff mode), which is induced by perturbations in the freestream. This mechanism mainly amplified the fluctuating energy within the low-frequency range, thereby diminishing the prominence of the K–H band energy. This non-modal instability is discussed later.

Although the K–H frequency represents the separated-flow transition mechanism, the spectral energy contained in low- and high-frequency ranges plays an important role as well. The unresolved unsteadiness represented by the RMS of velocity was decomposed into three parts by Eq. 7. Based on the K–H frequency bands (KH), the ranges lower and higher than those were defined as the low-frequency range (LF) and high-frequency range (HF), respectively. This approach makes it possible to quantify the kinetic energy associated with velocity fluctuations within specified frequency ranges. As shown in Fig. 12(a), it is evident that the development of the LF fluctuations in the boundary layer is similar to the overall fluctuations (as shown in Fig. 9). These fluctuations emerged before separation, grew rapidly in the separated shear layer along the inflection point (discussed later), and reached a maximum around the thickest part of the LSB. Meanwhile, the spectral energy within the K–H frequency bands became visible, as shown in Fig. 12(b), which is consistent with the results of Simoni et al. (2012). The difference is that Regions A and B are also observed in the spectral energy contours within the K–H bands. However, the PSD inside the bubble did not exhibit any dominant frequency, indicating that instability occurred over a broader frequency range as Fig. 13 shows. Close to the reattachment region, the HF spectral energy fluctuations become visible, implying that the reattachment process is associated with the breakdown of large-scale flow structures into small-scale structures. Furthermore, as shown in Fig. 12(c), the HF fluctuation cores moved upstream as *Re* increased. It can be inferred that *Re* evidently affects the transition stage at the rear part of the suction side, which agrees with the results shown in Fig. 7.

3.5 Inflection Instability and Growth Mechanisms

The boundary layer with an inflection point is considered unstable (Dovgal et al., 1994; Diwan & Ramesh, 2009). The inflection point and maximum u_{rms} positions, as determined by the spline-fitted velocity u and u_{rms} profiles, respectively, were close to the front part of the separated shear layer as Fig. 14 shows. This correlation holds for all *Re*. Diwan and Ramesh (2009) elucidated that

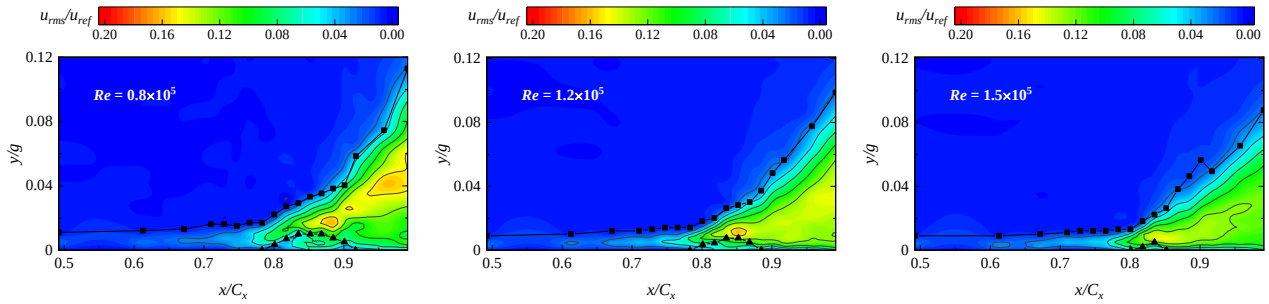

(a) Spectral energy within the low-frequency range

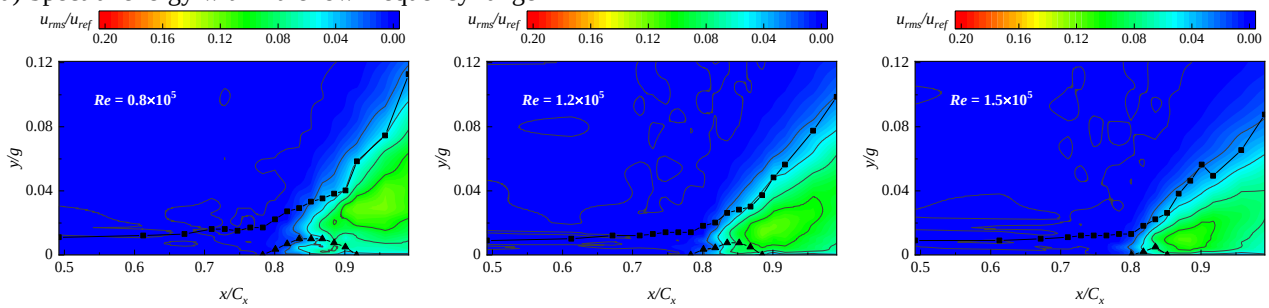

(b) Spectral energy within the K–H frequency bands

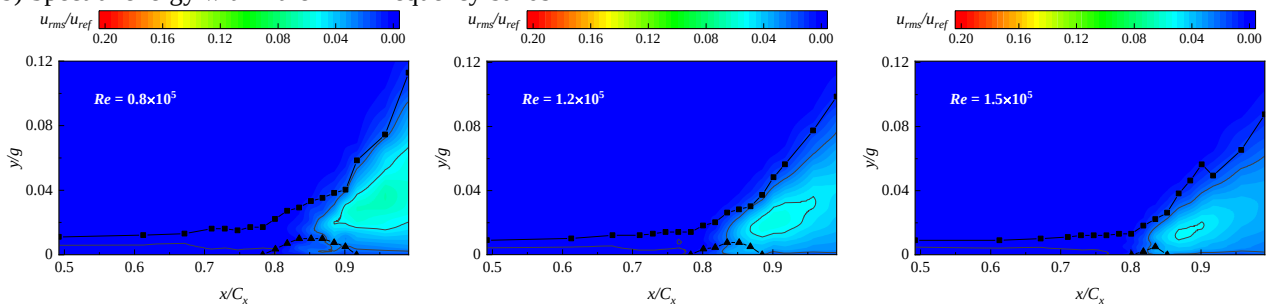

(c) Spectral energy within the high-frequency range

Fig. 12 Specific contributions of low-frequency, K–H frequency, and high-frequency energies to the overall unresolved unsteadiness with the boundary layer and LSB edges superimposed

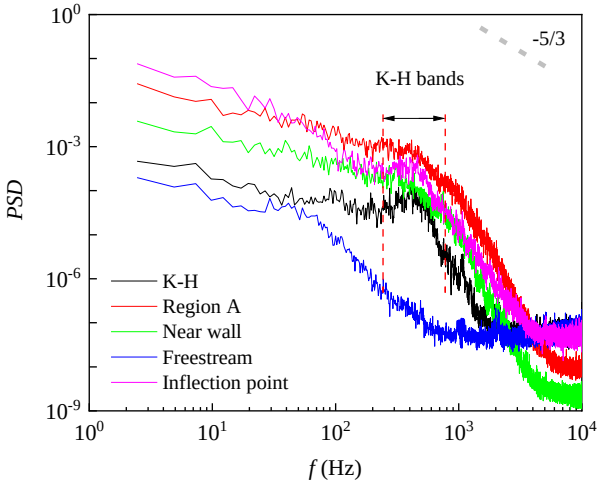

Fig. 13 Power spectral density at different positions along station 8 (*Re* = 0.8×10^5)

although the primary instability in an LSB is its inflection nature, the origin of which can be traced upstream. This explains why the near-wall inflection points preceding separation did not interact with the disturbances that penetrated the boundary layer through the "shear sheltering" effect. Only when the distance between the separated shear layer and wall is sufficiently large could the inflection instability be responsible for the substantial fluctuating energy enhancement. The maximum integrated spectral energy locations (represented by *max* u_{rms} as well) within the selected frequency ranges are shown in Fig. 16. It can be seen that the spectral energy within the K–H frequency bands corresponds best to inflection points, suggesting that although the inflection instability can amplify the fluctuating energy throughout the frequency domain, it remains inherently related to the inviscid K–H mechanism. Fig. 15. shows the chordwise variation in fluctuation energy, revealing an algebraic growth pattern downstream of the separation, which deviates from the linear stability theory. Jaroslawski et al. (2023) attributed this growth pattern to the increasing dominance of the non-modal instability associated with the low-frequency Klebanoff mode induced by the FST. A low constant growth rate of the disturbances prior to separation was observed under different *Re*. Therefore, the upstream disturbances did not significantly influence the separation locations. As *Re* increases, there is only a slightly larger growth rate of *max* u_{rms} in the separated shear layer, whereas a further increase in *Re* appears to have a limited effect (as indicated by the green dashed lines in Fig. 15). Finally, a breakdown occurs as the *max* u_{rms} approaches 20% of the local freestream velocity,

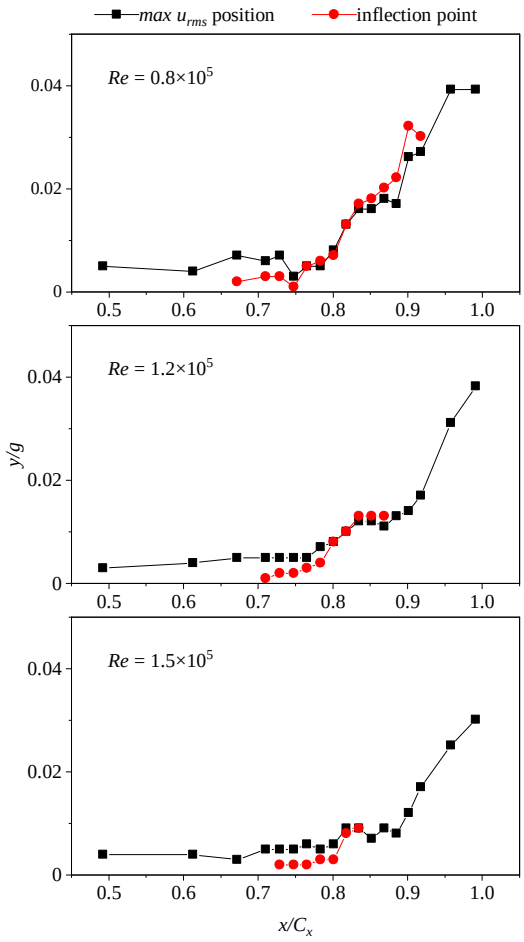

Fig. 14 Inflection point distribution and *max* u_{rms} locations in the boundary layer

which is consistent with the findings of Marxen et al. (2003) and Watmuff (1999). They concluded that the streamwise disturbances grow until the amplitude reached 10%~20% of the mainstream velocity.

The chordwise *max* u_{rms} variations integrated over the selected frequency ranges are shown in Fig. 17. This illustrates that the onset of the LF spectral energy growth corresponds to that of the K–H bands, both initiating around the separation point, whereas the HF spectral energy lags slightly behind. Furthermore, the energy within the K–H frequency bands underwent exponential amplification, confirming the presence of modal instability (K–H). The coexistence of modal instability

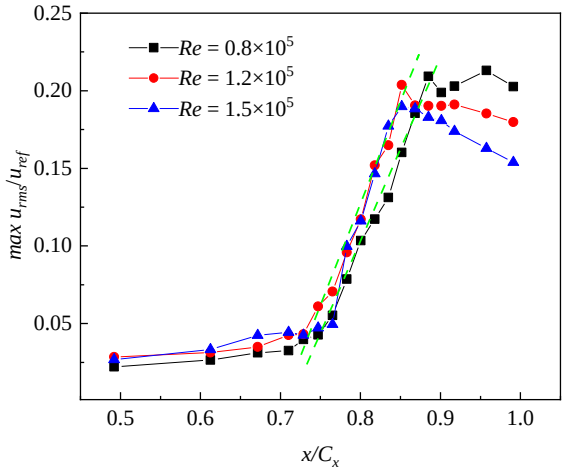

Fig. 15 *max* u_{rms} growth rate in the boundary layer

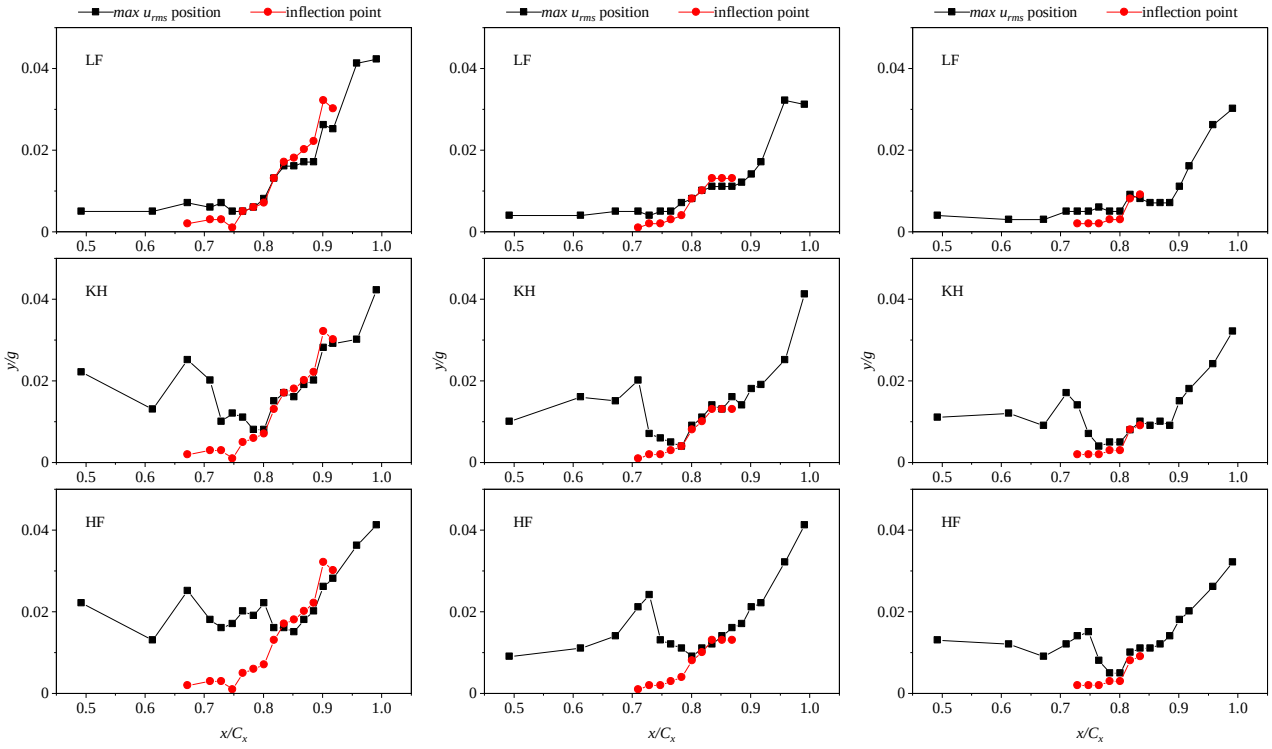

(a) Re = 0.8×10^5 (b) Re = 1.2×10^5 (c) Re = 1.5×10^5

Fig. 16 Inflection point distribution and *max* u_{rms} locations at different frequency ranges in the boundary layer

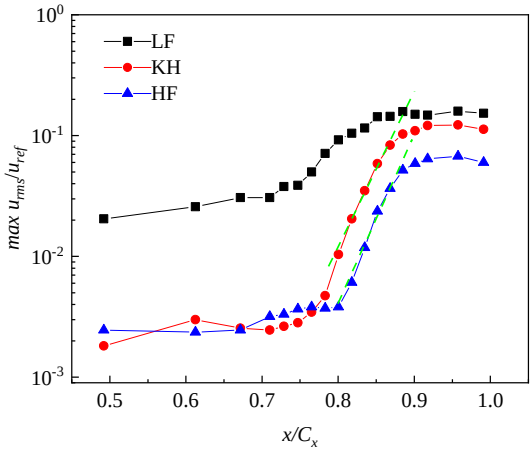

(a) Re = 0.8×10^5

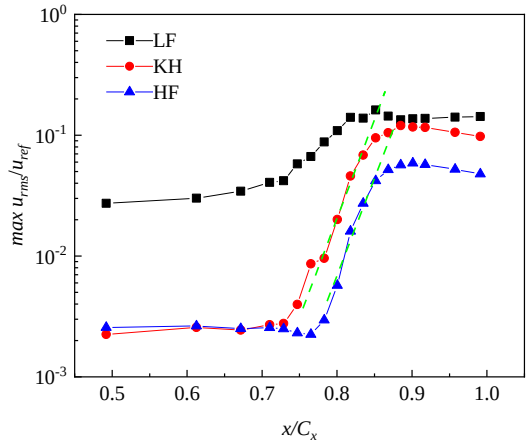

(b) Re = 1.2×10^5

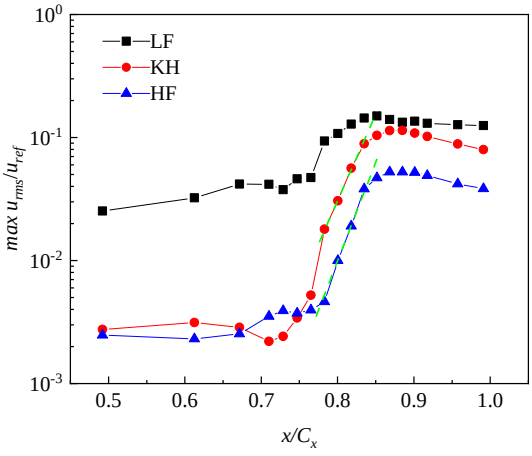

(c) Re = 1.5×10^5

Fig. 17 *max* u_{rms} growth rate within selected frequency ranges

raised by the separated shear layer and non-modal instability due to FST should be confirmed in the present experiments. However, the HF spectral energy also grows exponentially, which is not yet understood. The authors speculated that non-modal instability promotes a fast spectral energy transfer within the K–H frequency band to higher frequency ranges. Non-modal instability growth allows the spectral energy to spread over a broader bandwidth, which is also a typification of bypass transition.

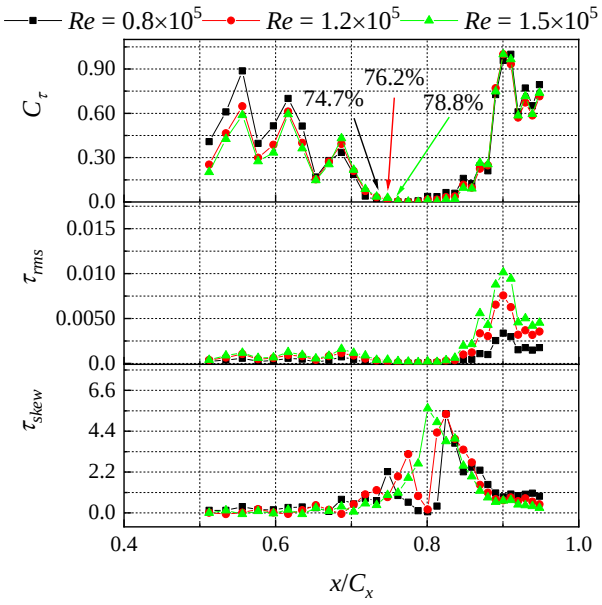

Fig. 18 Statistical results of the hot-film sensors

The existence of non-modal instability makes the present study different from that of Simoni et al. (2012), in which the onset of energy growth within the K–H bands is accompanied by energy saturation of the LF ranges. As shown in Fig. 17, there is no significant difference in the growth rate of the spectral energy between the KH and HF ranges, and both ranges show a larger rate than the LF range. This finding is consistent with those of Simoni et al. (2012). Non-modal instability leads to a faster breakdown of the K–H vortices (Jaroslawski et al., 2023). As Re increases, the separated shear layer moves closer to the wall. Consequently, the K–H instability is damped, and the non-modal instability (Klebanoff streaks) takes more responsibility for the increase in the fluctuating energy. A faster breakdown results in an earlier reattachment, which explains the Re effect on the reattachment point.

3.6 Hot-Film Tests

Fig. 18 shows the chordwise distributions of the normalized mean quasi-wall shear stress C_τ, root mean square τ_{rms}, and skewness τ_{skew}. The initial point of zero C_τ was considered to be the separation point, and the locations under different Re are 74.7%C_x, 76.2%C_x, and 78.8%C_x, respectively, which is consistent with the hot-wire measurements and the static pressure distributions. As seen from the τ_{rms} distributions, the most intense transition spreads to the wall at 90%C_x, in accordance with the largest C_τ value. Fig. 19 shows the raw voltage signals (Re = 0.8×10^5 used as a reference) that exhibit large-amplitude, low-frequency fluctuations corresponding to large-scale structures during the transition at 90%C_x. Conversely, as it approaches 93.9%C_x the signal decreases in amplitude and increases in frequency, characteristic of "breakdown." The hot-film signal evolution was similar to that reported by Liang et al. (2015). However, Re did not appear to play a role in this process, which requires further investigation. It is noteworthy that for the two lower Re there is a region of enlarged τ_{skew} before 80%C_x, but this cannot be described as a transitional signal. As these regions are close to the separation points, they are caused

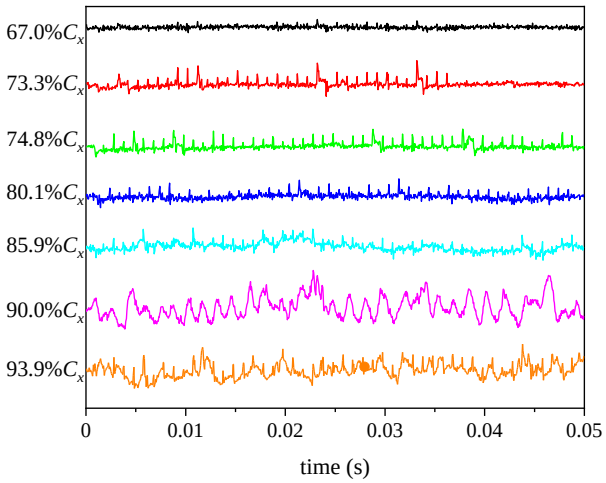

Fig. 19 Raw signals of the hot-film at different axial positions (Re = 0.8×10^5)

by laminar fluctuations, as discussed by Mahallati et al. (2012). Additionally, the raw data in Fig. 19 prove this because of the larger positive signal amplitudes at 74.8%C_x compared to those at 80.1%C_x, which is not a typical development in transitional flow. τ_{skew} increases around 81.3%C_x, reaching a peak at 82.5%C_x at Re = 0.8×10^5, which is in line with the area of Region A. Therefore, this represents the near-wall disturbances identified by the hot-film sensors. When Re increases to 1.5×10^5, the LSB is shortened, and laminar fluctuations around the separation point emerge with transitional fluctuations, as shown in Fig. 18. In conclusion, although the hot-film can compensate for the deficiency of near-wall measurements by hot-wire probes, the information provided by the hot-film may overlap for a complex separated-flow transition, making interpretation difficult.

Hot-film sensors are effective for identifying separation points. However, in the cases of separated-flow transition involving two disturbance regions, the transitional signal detected by the hot-film is close to the wall, making it challenging to discriminate the transitional information within the separated shear layer. Until breakdown occurred or the boundary layer approached the late transition stage, the hot-wire and hot-film measurements yielded similar results.

4. CONCLUSION

In this study, it was found that a high-lift blade can substantially enhance the loading level. However, it also causes a greater profile loss due to the LSB on the suction side, which is typically accompanied by a laminar-turbulent transition. Therefore, detailed experiments were conducted to investigate the separated boundary layers using both hot-wire and hot-film anemometers. Based on the results, the main conclusions of this study can be summarized as follows.

A higher Re only marginally delays separation, but significantly advances reattachment, resulting in a difference in the boundary layer state at the trailing edge. Two instability regions were observed on the high-lift blade surface: one located within the separated shear layer and the other in the reversed-flow inside the LSB, which is in agreement with experimental and computational studies for a flat-plate boundary layer. The dominant frequency of the external instability confirms its association with the inviscid K–H mechanism, and $Sr_{\theta s}$ remains nearly constant as Re changes. The disturbances inside the reversed-flow were generated through viscous instability, not absolute instability, and the fluctuating energy spread over a broad frequency range. Interestingly, according to the present experimental results, even a low reversal level can trigger viscous instability.

In the presence of moderate FST intensity, the present study provide evidence of the coexistence of modal and non-modal instabilities, both initiating from the separation point. The predominant spectral energy of the non-modal instability was within the LF range and evolved at a lower growth rate than that of the K–H frequency band. Due to its LF energy, non-modal instability influences the spectrum of the disturbance within the separated shear layer, rendering the K–H frequency signal inconspicuous around the inflection point. The inviscid inflection in nature induced by the LSB amplifies not only the K–H instability but also the fluctuating energy within the LF range, and its origin can be traced to the disturbance penetrating the boundary layer through the "shear sheltering" effect. However, inflectional instability remains associated with the K–H mechanism, which cannot be bypassed, even with a thinner LSB at the highest Re.

Hot-film sensors can precisely indicate separation points. However, in a complex separated boundary layer, particularly one with two disturbed regions (inside and outside the LSB), the hot-film data mainly reflect near-wall disturbances. This explains the discrepancy between the hot-wire and hot-film test results.

The variation in FST should be considered in future experiments, with a combination of high-fidelity numerical simulations (LES or DNS), possibly achieving deeper insights into such flow dynamics.

ACKNOWLEDGEMENTS

The authors would like to thank the AECC Commercial Aircraft Engine Co., Ltd. for the project. We also thank the technical staff at the laboratory for their help with the experiments. Dalian Hanghua Technology Co., Ltd provided the hot-wire anemometer system, which is gratefully acknowledged.

CONFLICT OF INTEREST

The authors report no competing interest.

AUTHORS CONTRIBUTION

S. Yang: conceptualization; methodology; investigation; formal analysis; preparing figures; writing the original draft. **F. Tian**: conceptualization; methodology; investigation. **C. Teng**: the investigation. **B.**

Xu: funding acquisition; supervision; reviewing, and editing.

REFERENCES

Alam, M., & Sandham, N. D. (2000). Direct numerical simulation of "short" laminar separation bubbles with turbulent reattachment. *Journal of Fluid Mechanics*, *410*, 1–28. https://doi.org/10.1017/S0022112099008976

Balzer, W., & Fasel, H. F. (2016). Numerical investigation of the role of free-stream turbulence in boundary-layer separation. *Journal of Fluid Mechanics*, *801*, 289–321. https://doi.org/10.1017/jfm.2016.424

Bolinches-Gisbert, M., Robles, D. C., Corral, R., & Gisbert, F. (2020). Prediction of reynolds number effects on low-pressure turbines using a high-order ILES method. *Journal of Turbomachinery*, *142*(3), 031002. https://doi.org/10.1115/1.4045776

BIPM, IEC, IFCC, ILAC, ISO, IUPAC, IUPAP, &OIML. (2008). Evaluation of measurement data—Guide to the expression of uncertainty in measurement. Joint Committee for Guides in Metrology, JCGM 100:2008. https://doi.org/10.59161/JCGM100-2008E

Brinkerhoff, J. R., & Yaras, M. I. (2011). Interaction of viscous and inviscid instability modes in separation–bubble transition. *Physics of Fluids*, *23*(12), 124102. https://doi.org/10.1063/1.3666844

Coull, J. D., & Hodson, H. P. (2011). Unsteady boundary-layer transition in low-pressure turbines. *Journal of Fluid Mechanics*, *681*, 370–410. https://doi.org/10.1017/jfm.2011.204

Davies, M. R. D., & Duffy, J. T. (1995, June 5-8). *A semi-empirical theory for surface mounted aerodynamic wall shear stress gauges*. ASME 1995 International Gas Turbine and Aeroengine Congress and Exposition, Houston, Texas, USA. https://doi.org/10.1115/95-GT-193

Denton, J. D. (1993). The 1993 IGTI scholar lecture: loss mechanisms in turbomachines. *Journal of Turbomachinery*, *115*(4), 621–656. https://doi.org/10.1115/1.2929299

Diwan, S. S., & Ramesh, O. N. (2009). On the origin of the inflectional instability of a laminar separation bubble. *Journal of Fluid Mechanics*, *629*, 263–298. https://doi.org/10.1017/S002211200900634X

Dovgal, A. V., Kozlov, V. V., & Michalke, A. (1994). Laminar boundary layer separation: Instability and associated phenomena. *Progress in Aerospace Sciences*, *30*(1), 61–94. https://doi.org/10.1016/0376-0421(94)90003-5

Satta, F., Simoni, D., Ubaldi, M., Zunino, P., & Bertini, F. (2014). Loading distribution effects on separated flow transition of ultra-high-lift turbine blades. *Journal of Propulsion and Power*, *30*(3), 845–856. https://doi.org/10.2514/1.B34968

Funazaki, K., Yamada, K., Tanaka, N., & Chiba, Y. (2009, June 8-12). *Detailed studies on separated boundary layers over low-pressure turbine airfoils under several high lift conditions: Effect of freestream turbulence*. ASME Turbo Expo 2009: Power for Land, Sea, and Air, Orlando, Florida, USA. https://doi.org/10.1115/GT2009-59813

Gaster, M. (1967). The structure and behaviour of laminar separation bubbles. *Aeronautical Research Council Reports and Memoranda*, No. 5395. https://citeseerx.ist.psu.edu/document?repid=rep1&type=pdf&doi=f1579f637cc7eefb938a4ffd6613b4d46298e086

Hain, R., Kähler, C. J., & Radespiel, R. (2009). Dynamics of laminar separation bubbles at low-Reynolds-number aerofoils. *Journal of Fluid Mechanics*, *630*, 129–153. https://doi.org/10.1017/S0022112009006661

Ho, C. M., & Huerre, P. (1984). Perturbed Free Shear Layers. *Annual Review of Fluid Mechanics*, *16*(1), 365–422. https://doi.org/10.1146/annurev.fl.16.010184.002053

Hodson, H. P. (1985). Measurements of wake-generated unsteadiness in the rotor passages of axial flow turbines. *Journal of Engineering for Gas Turbines and Power*, *107*(2), 467–475. https://doi.org/10.1115/1.3239751

Hodson, H., & Howell, R. (2005). The role of transition in high-lift low-pressure turbines for aeroengines. *Progress in Aerospace Sciences*, *41*, 419–454. https://doi.org/10.1016/j.paerosci.2005.08.001

Hosseinverdi, S., & Fasel, H. F. (2019). Numerical investigation of laminar–turbulent transition in laminar separation bubbles: The effect of free-stream turbulence. *Journal of Fluid Mechanics*, *858*, 714–759. https://doi.org/10.1017/jfm.2018.809

Howell, R. J., Hodson, H. P., Schulte, V., Stieger, R. D., Schiffer, H. P., Haselbach, F., & Harvey, N. W. (2002). Boundary layer development in the BR710 and BR715 LP turbines—the implementation of high-lift and ultra-high-lift concepts. *Journal of Turbomachinery*, *124*(3), 385–392. https://doi.org/10.1115/1.1457455

Howell, R. J., Ramesh, O. N., Hodson, H. P., Harvey, N. W., & Schulte, V. (2000). high lift and aft-loaded profiles for low-pressure turbines. *Journal of Turbomachinery*, *123*(2), 181–188. https://doi.org/10.1115/1.1350409

Ikeya, Y., Örlü, R., Fukagata, K., & Alfredsson, P. H. (2017). Towards a theoretical model of heat transfer for hot-wire anemometry close to solid walls. *International Journal of Heat and Fluid Flow*, *68*, 248–256. https://doi.org/10.1016/j.ijheatfluidflow.2017.09.002

Istvan, M. S., & Yarusevych, S. (2018). Effects of free-stream turbulence intensity on transition in a laminar separation bubble formed over an airfoil. *Experiments*

in Fluids, *59*(3), 52. https://doi.org/10.1007/s00348-018-2511-6

Lin, J. M., & Pauley, L. L. (1996). Low-Reynolds-number separation on an airfoil. *AIAA Journal*, *34*(8), 1570–1577. https://doi.org/10.2514/3.13273

Jacobs, R. G., & Durbin, P. A. (2001). Simulations of bypass transition. *Journal of Fluid Mechanics*, *428*, 185–212. https://doi.org/10.1017/S0022112000002469

Jaroslawski, T., Forte, M., Vermeersch, O., Moschetta, J.-M., & Gowree, E. R. (2023). Disturbance growth in a laminar separation bubble subjected to free-stream turbulence. *Journal of Fluid Mechanics*, *956*, A33. https://doi.org/10.1017/jfm.2023.23

Lang, M., Rist, U., & Wagner, S. (2004). Investigations on controlled transition development in a laminar separation bubble by means of LDA and PIV. *Experiments in Fluids*, *36*(1), 43–52. https://doi.org/10.1007/s00348-003-0625-x

Li, H., & Yang, Z. (2016, June). *Numerical study of separated boundary layer transition under pressure gradient*. 12th International Conference on Heat Transfer, Fluid Mechanics and Thermodynamics, Malaga, Spain. https://repository.up.ac.za/handle/2263/61901

Liang, Y., Zou, Z. P., Liu, H. X., & Zhang, W. H. (2015). Experimental investigation on the effects of wake passing frequency on boundary layer transition in high-lift low-pressure turbines. *Experiments in Fluids*, *56*(4), 81. https://doi.org/10.1007/s00348-015-1947-1

Mahallati, A., McAuliffe, B. R., Sjolander, S. A., & Praisner, T. J. (2012). Aerodynamics of a low-pressure turbine airfoil at low reynolds numbers—part i: steady flow measurements. *Journal of Turbomachinery*, *135*(1). https://doi.org/10.1115/1.4006319

Marxen, O. (2020, January 6-10). *Viscous-inviscid interaction in laminar separation bubbles (invited)*. *AIAA Scitech 2020 Forum*, Orlando, FL. https://doi.org/10.2514/6.2020-1555

Marxen, O., Lang, M., Rist, U., & Wagner, S. (2003). A Combined experimental/numerical study of unsteady phenomena in a laminar separation bubble. *Flow, Turbulence and Combustion*, *71*(1–4), 133–146. https://doi.org/10.1023/B:APPL.0000014928.69394.50

Mayle, R. E. (1991). The role of laminar-turbulent transition in gas turbine engines. *Journal of Turbomachinery*, *113*(4), 509–536. https://doi.org/10.1115/1.2929110

Mcauliffe, B. (2007). *Transition in separation bubbles: Physical mechanisms and passive control techniques*. Carleton University. https://doi.org/10.22215/etd/2007-06692

McAuliffe, B. R., & Yaras, M. I. (2005, June 6-9). *Separation-bubble-transition measurements on a Low-Re airfoil using particle image velocimetry*. ASME Turbo Expo 2005: Power for Land, Sea, and Air, Reno, Nevada, USA. https://doi.org/10.1115/GT2005-68663

McAuliffe, B. R., & Yaras, M. I. (2008). Numerical study of instability mechanisms leading to transition in separation bubbles. *Journal of Turbomachinery*, *130*(2). https://doi.org/10.1115/1.2750680

McAuliffe, B. R., & Yaras, M. I. (2010). Transition mechanisms in separation bubbles under low- and elevated-freestream turbulence. *Journal of Turbomachinery*, *132*(1), 011004. https://doi.org/10.1115/1.2812949

Ripley, M. D., & Pauley, L. L. (1993). The unsteady structure of two-dimensional steady laminar separation. *Physics of Fluids A: Fluid Dynamics*, *5*(12), 3099–3106. https://doi.org/10.1063/1.858719

Rist, U., & Maucher, U. (2002). Investigations of time-growing instabilities in laminar separation bubbles. *European Journal of Mechanics - B/Fluids*, *21*(5), 495–509. https://doi.org/10.1016/S0997-7546(02)01205-0

Roberts, S. K., & Yaras, M. I. (2005). Large-eddy simulation of transition in a separation bubble. *Journal of Fluids Engineering*, *128*(2), 232–238. https://doi.org/10.1115/1.2170123

Rodríguez, D., & Gennaro, E. M. (2019). Enhancement of disturbance wave amplification due to the intrinsic three-dimensionalisation of laminar separation bubbles. *The Aeronautical Journal*, *123*(1268), 1492–1507. https://doi.org/10.1017/aer.2018.115

Rodríguez, D., Gennaro, E. M., & Juniper, M. P. (2013). The two classes of primary modal instability in laminar separation bubbles. *Journal of Fluid Mechanics*, *734*, R4. https://doi.org/10.1017/jfm.2013.504

Rodríguez, D., Gennaro, E. M., & Souza, L. F. (2021). Self-excited primary and secondary instability of laminar separation bubbles. *Journal of Fluid Mechanics*, *906*, A13. https://doi.org/10.1017/jfm.2020.767

Simoni, D., Ubaldi, M., Zunino, P., Lengani, D., & Bertini, F. (2012). An experimental investigation of the separated-flow transition under high-lift turbine blade pressure gradients. *Flow, Turbulence and Combustion*, *88*(1–2), 45–62. https://doi.org/10.1007/s10494-011-9375-7

Singh, N. K. (2019). Instability and transition in a laminar separation bubble. *Journal of Applied Fluid Mechanics*, *12*(5), 1511–1525. https://doi.org/10.29252/jafm.12.05.29607

Spalart, P. R., & Strelets, M. K. (2000). Mechanisms of transition and heat transfer in a separation bubble. *Journal of Fluid Mechanics*, *403*, 329–349. https://doi.org/10.1017/S0022112099007077

Sun, S., Wu, X., Tan, T., Zuo, C., Pan, S., & Liu, F. (2020, September 21-25). *Generation and development of*

klebanoff streaks in low-pressure turbine cascade under upstream wakes. ASME Turbo Expo 2020: Turbomachinery Technical Conference and Exposition, Virtual, Online. https://doi.org/10.1115/GT2020-15313

Talan, M., & Hourmouziadis, J. (2002). Characteristic regimes of transitional separation bubbles in unsteady flow. *Flow, Turbulence and Combustion*, *69*(3), 207–227. https://doi.org/10.1023/A:1027355105017

Volino, R. J. (2002a). Separated flow transition under simulated low-pressure turbine airfoil conditions—Part 1: Mean flow and turbulence statistics. *Journal of Turbomachinery*, *124*(4), 645–655. https://doi.org/10.1115/1.1506938

Volino, R. J. (2002b). Separated flow transition under simulated low-pressure turbine airfoil conditions—Part 2: Turbulence spectra. *Journal of Turbomachinery*, *124*(4), 656–664. https://doi.org/10.1115/1.1506939

Volino, R. J., & Bohl, D. G. (2004, June 14-17). *Separated flow transition mechanism and prediction with high and low freestream turbulence under low pressure turbine conditions*. ASME Turbo Expo 2004: Power for Land, Sea, and Air, Vienna, Austria. https://doi.org/10.1115/gt2004-53360

Walker, G. J. (1989). Transitional flow on axial turbomachine blading. *AIAA Journal*, *27*(5), 595–602. https://doi.org/10.2514/3.10150

Watmuff, J. H. (1999). Evolution of a wave packet into vortex loops in a laminar separation bubble. *Journal of Fluid Mechanics*, *397*, 119–169. https://doi.org/10.1017/S0022112099006138

Yang, S., Xu, B., Tian, F., & Wang, B. (2023). Aerodynamic performance of high-lift blades in low-pressure turbines with periodic upstream wakes. *Journal of Mechanical Science and Technology*, *37*(5), 2425–2437. https://doi.org/10.1007/s12206-023-0419-4

Yang, Z. (2019). On bypass transition in separation bubbles: A review. *Propulsion and Power Research*, *8*(1), 23–34. https://doi.org/10.1016/j.jppr.2018.12.004

Yang, Z., & Voke, P. R. (2001). Large-eddy simulation of boundary-layer separation and transition at a change of surface curvature. *Journal of Fluid Mechanics*, *439*, 305–333. https://doi.org/10.1017/S0022112001004633

Zaki, T. A., & Durbin, P. A. (2005). Mode Interaction and the Bypass Route to Transition. *Journal of Fluid Mechanics*, *531*, 85–111. https://doi.org/10.1017/S0022112005003800

Zaki, T. A., & Durbin, P. A. (2006). Continuous mode transition and the effects of pressure gradient. *Journal of Fluid Mechanics*, *563*, 357–388. https://doi.org/10.1017/S0022112006001340

Zhang, X., Mahallati, A., & Sjolander, S. (2002, July 7-10). *Hot-film measurements of boundary layer transition, separation and reattachment on a low-pressure turbine airfoil at low reynolds numbers*. 38th AIAA/ASME/SAE/ASEE Joint Propulsion Conference & Exhibit, Indianapolis, Indiana. https://doi.org/10.2514/6.2002-3643

Zhao, Y., & Sandberg, R. D. (2020). Bypass transition in boundary layers subject to strong pressure gradient and curvature effects. *Journal of Fluid Mechanics*, *888*, A4. https://doi.org/10.1017/jfm.2020.39